Single Molecule Level Studies of Reversible Ligand Binding to Metal Porphyrins at the Solution/Solid Interface [J. Porphyrins and Phthalocyanines 2019]

Ursula Mazur* and K. W. Hipps

Department of Chemistry and Materials Science and Engineering Program, Washington State University, Pullman, Washington 99164-4630

ABSTRACT: Ligands bind reversibly to metal porphyrins in processes such as molecular recognition, electron transport and catalysis. These chemically relevant processes are ubiquitous in biology and are important in technological applications. In this article, we focus on the current advances in ligand binding to metal porphyrin receptors noncovalently bound at the solution/solid interface. In particular, we restrict ourselves to studies at the single molecule level. Dynamics of the binding/dissociation process can be monitored by scanning tunneling microscopy (STM) and can yield both qualitative and quantitative information about ligand binding affinity and the energetics that define a particular ligation reaction. Molecular and time dependent imaging can establish whether the process under study is at equilibrium. Ligand concentration dependent studies have been used to determine adsorption isotherms and thermodynamic data for processes occurring at the solution/solid interface. In several binding reactions, the solid support acted as an electron-donating fifth coordination site thereby significantly changing the metal porphyrin receptor's affinity for exogenous ligands. Supporting calculations provide insight into the metalloporphyrin/support and ligand–metalloporphyrin/support interactions and their energetics.

Keywords: porphyrins, reversible ligand binding, solution/solid interface, isotherms, kinetics, thermodynamics, STM, EC-STM, DFT calculations

*Correspondence to: Ursula Mazur, ORCID: Ursula Mazur: 0000-0002-3471-4883, email: umazur@wsu.edu; K. W. Hipps, K. W. Hipps: 0000-0002-5944-5114, email: hipps@wsu.edu

INTRODUCTION

Noncovalent (reversible) ligand binding to metalloporphyrin receptors plays an essential role in many biologically and technologically relevant processes. Cytochromes transfer electrons [1], myoglobin and hemoglobin transport and store oxygen [2,3], while enzymes reversibly bind their substrates as part of catalytic cycles [4,5]. Artificial metal porphyrins are known to imitate the natural binding processes and are being exploited for separating gas mixtures [6], energy storage and delivery [7,8], selective chemical sensing [2], cancer therapeutics [9,10], and catalysis [11,12]. There continues to be a tremendous interest in these chemically relevant responses especially in determining the pathways leading to ligand binding to the porphyrin receptors and the thermodynamic and kinetic properties of a ligand–receptor pair.

The ensemble level chemistry of ligand binding is typically probed by methods such as electronic spectroscopy, electrochemistry, electron paramagnetic resonance and nuclear magnetic resonance spectroscopy. However, extracting correct mechanisms from these ensemble measurements is extremely difficult. Ensemble methods can provide data on the concentration and temperature evolution of the system on a relatively fast time scale, but methods that allow direct molecular scale monitoring (like scanning tunneling microscopy, STM) can provide more definitive mechanistic insights. With STM, it is possible to monitor single molecules (and parts of molecules) [13-15] while they participate in multistep chemical reactions and to identify reactants, intermediates and products. STM methodology allows simultaneous access to spatial, temporal, and intra– and intermolecular reaction dynamics, which may provide unique information about reaction mechanisms that remains hidden in ensemble measurements at the macroscopic scale.

Metal porphyrin axial coordination to small ligands at the single molecule level has been demonstrated in the controlled environment of an ultra-high vacuum STM (UHV-STM) [16- 23]. More recently, experiments have been carried out on reactions involving a single porphyrin receptor binding a single ligand at the solution/solid interface [24- 32]. This chemistry is new and its growing success can be attributed in part to the remarkable stability of the metal porphyrin receptor monolayers at the solution/solid interface near room temperature. For example, Bhatari at al. reported that octaethylporphyrin (OEP) substituted with cobalt or nickel did not desorb from conductive substrates in phenyl octane solutions until about 70 °C [33,34]. Although most STM based ligand binding studies reported individual images to qualitatively verify ligand-receptor binding events, few recorded sequential images of the binding processes as a function of time for quantitative analysis. These latter investigations exploited time dependent microscopic ligand binding imaging data to extract reaction rates, equilibrium constants and thermodynamic quantities and related these results to available ensemble averages data.

In this review article, we survey recent developments in STM studies of reversible ligand binding chemistry to metal porphyrin monolayers adsorbed on conducting surfaces in solution and in electrochemical environments (studied by electrochemical STM, EC-STM). The ligating molecules of interest are biologically and chemically relevant and include O_2 and nitrogen bases such as imidazole and pyridine derivatives. The porphyrin receptors are substituted with first row transition metal elements and self-assembled on different conducting substrates. We highlight temperature and concentration dependent imaging experiments from which thermodynamic parameters were extracted and identify examples of ligand binding chemistry unique to the surface supported receptors. For

some experiments, the metalloporphyrin/support and ligand–metalloporphyrin/support interactions were further explored with theoretical calculations. Theory based energetics for these interactions were also extracted. In the final segment of this review, we recap the current progress and identify the future prospects of binding studies at the single molecule level**.**

STM experiments at the solution/solid interface are typically performed in nonconducting low vapor pressure organic solvents although aqueous solutions can also be used. Highly ordered pyrolytic graphite (HOPG) or Au(111) serve as prototypical substrates. Etched or cut Pt/Ir, tungsten or gold wires usually function as scanning probes, although imaging in aqueous solvents requires special coated tips for minimizing Faradaic currents. Imaging can be accomplished under ambient conditions by simply immersing the tip (probe) in a small volume (few μL) of liquid placed on a substrate. For carrying out experiments under controlled conditions using a setup such as the one depicted in Fig. 1 is more appropriate. Here, the entire STM experiment is housed in an environmental chamber outfitted with gas inlets and outlets. A sample cell fabricated from nonreactive material (e.g. Teflon) mounted on a substrate is in contact with a Peltier heating/cooling stage that can control temperature in the range of −10 °C to 150 °C. A more advanced STM system for working with high vapor pressure solvents and operable at variable temperatures and pressures was recently developed by Hipps and coworkers and is reported in the literature [35]. STM experiments at the solution/solid interface can also be carried out in an electrochemical environment by employing an electrochemical scanning tunneling microscope. In an EC-STM, two additional electrodes are required to control the electrochemical potentials; a reference electrode can also be employed.

REVERSIBLE OXYGEN BINDING to Mn, Co and Cu PORPHYRINS

Perhaps the most studied reversible binding reaction to metal porphyrin receptors concerns the dioxygen ligand. The binding of O_2 is the first step in many important processes, such as cellular respiration, corrosion, and catalysis. De Feyter and Elemans observed the formation of different manganese oxo species when the oxygen in air reacted with Mn porphyrin (Fig. 2) monolayer at the octanoic acid/Au(111) interface [23,24,36]. The molecular products were identified by their apparent height (relative conductivity) in the STM images as seen in Fig. 2b. Thus, the brightest feature labeled **1,** was attributed to a double-decker Mn^{III}–O–Mn^{III} complex, while adjacent molecules were assigned to Mn^{II} (**2**), Mn^{III}–Cl (**3**) and Mn^{II}=O (**4**), respectively. These molecular features appeared after a 10-minute exposure of the parent porphyrin (Figure 2a) to air and their concentration continued to evolve reversibly for several hours. It was noted that a single molecule of O_2 usually oxidized two adjacent Mn^{II} porphyrins forming two Mn^{II}=O (**4**) adducts in a cooperative manner [24]. The interaction between the porphyrin adsorbate and the Au(111) substrate was implicated not only in the cooperative effect that produced the neighboring Mn^{II}=O species but also in other products resulting from the reaction of *meso*-5,10,15,20-tetrakis[4-(*R,R,R,R*)-2-*N*-ctadecyl-amidoethyloxyphenyl]porphyrin Mn(III) chloride (Mn1Cl, Fig. 2) and O_2 at the solution/solid interface.

The first STM study that provided a quantitative description of a reversible ligand binding to a metal porphyrin at the solution/solid interface was performed by Friesen and coworkers [26,37,38]. These researchers demonstrated for the first time that thermodynamic values can be extracted from microscopic STM data. In particular, they studied the binding of O_2 to cobalt(II) octaethyl porphyrin, CoOEP, at the phenyloctane/HOPG interface. Oxygen partial

pressure, temperature, and time were all treated as experimental parameters. While the binding of dioxygen to simple cobalt porphyrins is well known, this reaction typically occurs at temperatures well below 20 °C. Cobalt substituted myoglobins and cobalt "picket fence" porphyrin are known to reversibly bind O_2 in solution under ambient conditions but only when a basic axial ligand is present [39]. In fluid solution or in glasses, CoOEP will not bind oxygen at temperatures above 173 K (Fig. 3a). However, it is known that oxygen binding to cobalt porphyrins can be enhanced by axial coordination to a basic axial ligand (such as imidazole) at the position opposite to O_2 binding. Friesen demonstrated that CoOEP displayed enhanced oxygen binding depending upon the substrate chosen [26].

CoOEP molecules on HOPG imaged in deoxygenated phenyl octane appeared bright (Fig. 3b) due to tunneling through half-filled d_z^2 orbital in the cobalt species. When O_2 was introduced, some molecules turned dim, (Fig. 3c). These dim molecules were identified as those binding O_2 (as O_2^-). STM images of a given area collected with time generated a movie with molecules that appear to blink on and off. Each frame was analyzed for the fraction, Θ, of dark molecules, and the values were plotted versus time, Fig. 4. In the two sequential images in that figure, all the dim molecules have been indicated with a white circle in the first frame. In the second image, those molecules that were dim in the previous image and remain dim are shown in white; the blue circles indicate dim molecules that were bright in the previous image. The scatter in the Θ data is consistent with the expected statistical fluctuation of a small sample. From this data, it is clear that the system is in dynamic equilibrium. Furthermore, changing the oxygen partial pressure over the solution shifted the equilibrium in concert. Thus, the system was in thermodynamic equilibrium. Time averages collected for several partial pressures followed the Langmuir isotherm, which provided an equilibrium constant for the oxygen binding (Fig. 5). By measuring isotherms at various temperatures ranging from 10 °C to 40 °C, $\Delta G°(T)$ was obtained. Using standard thermodynamic relationships $\Delta H° = -87\pm10$ kJ/mole and $\Delta S° = 339\pm30$ J/K-mol were calculated; these values were comparable to those obtained from porphyrins chemically designed to bind oxygen in solution at room temperature [26].

Friesen had quantitatively demonstrated that the HOPG solid support acted in a manner similar to an electron–donating ligand bound to the fifth coordination site on the cobalt ion of CoOEP, thereby greatly increasing the receptor's affinity for oxygen. Later, Hipps and Mazur showed that the extent of oxygen binding by CoOEP changes dramatically with substrate, in the order MoS_2 > HOPG > Au [37]. They have tentatively associated this binding trend with the work function of the substrate. Thus, gold with the largest work function was the poorest a donor, while MoS_2 with the smallest work function was the best electron donor and oxygen most readily ligated the CoOEP supported on that substrate [37].

The interaction of oxygen with Co substituted porphyrins (and phthalocyanines) during a redox process has been examined extensively in electrochemical environments [40- 45]. Several researchers performed *in-situ* EC-STM studies of oxygen reduction reaction (ORR) catalyzed by cobalt porphyrins in 0.1 M solutions of $HClO_4$ [27,46], KOH and $NaClO_4$ [47] using Au(111) as a substrate. It is important to note that the imaging results of oxygen binding to cobalt ions in these complex ionic solutions were different from the STM data obtained for O_2 interaction with Co porphyrins in nonaqueous solvents without potential control [26,37,38]. The latter were discussed in the previous paragraphs.

Images of pure CoTPP monolayers acquired in an acid solution (without applied potential) [27] presented bright (high) features consistent with a number of previous studies demonstrating that tunneling through the half filled d_z^2 orbital produces the bright molecular center [13,26,48]. In a basic environment, however, cobalt porphyrin cores consisted of two bright spots that were attributed to a CoTPP−OH^- complex [47].

EC-STM images of CoTPP monolayers collected in oxygen-saturated 0.1M $HClO_4$ solutions under applied potential (positive) exhibited two types of molecules: bright and dim. The molecules with the high contrast were identified as transient CoTPP–O_2 complexes while the dimmer molecules were assigned to the CoTPP parent [27,46]. The numbers of the CoTPP–O_2 species varied monotonically with oxygen concentration and reverted to the CoTPP parent when the potential was negative. This process was completely reversible and did not take place when oxygen was replaced with an inert gas. In alkaline solutions, only trace amount of the high-contrast CoTPP–O_2 species were also detected in the STM images. These interpretations are not consistent with optical and electron paramagnetic resonance spectroscopy, EPR, work.

Several groups reported ORR studies indicating that oxygen binding to Co(II) porphyrins was most effective in high pH. These studies were based on optical and EPR, results [39-41,43,44]. While the EPR clearly indicated the formation of a Co^{III}–$O_2^{\bullet-}$ adduct under aerobic conditions in high pH solutions, addition of a strong acid resulted in the rapid disappearance of most of the EPR signal. Colleman [39,40] and Stahl [41] concluded that more acidic conditions accelerated the decomposition of the oxygen cobalt adduct.

Effects of oxygen on the Cu(II) porphyrin monolayer at the dichlorobenzene/HOPG interface were reported by Salmeron and coworkers [28]. These researchers observed that CuOEP monolayers deposited from an oxygen treated solution exhibited a nearly rectangular lattice. However, when adsorbed from an oxygen free solution, the same metal porphyrin formed an oblique lattice, an organization common for metalloporphyrins adsorbed on HOPG. Combined Raman and the STM experiments led to a proposal that the oxygen molecules bind to the Cu center of the CuOEP molecules and thus modify the surface structure of the porphyrin monolayer.

REVERSIBLE NITROGENEOUS BASES BINDING to Ni and Zn PORPHYRINS

The binding of nitrogen bases to metal porphyrins directly facilitates molecular recognition or sensing and enables enzymatic transformations. Synthetic nickel porphyrins readily form six-coordinated adducts with two axial ligands and have been extensively used as model systems for investigating the dynamics of binding of basic ligands, because, unlike cobalt and iron, nickel ion does not bind exogenous ligands such as CO and O_2 [49,50]. In myoglobin and hemoglobin, for example, an imidazole coordinated opposite to O_2 is required for oxygen to bind to the iron centers [51].

Nandi et al. studied support–induced chemistry in the reaction of imidazole (Im) with NiOEP/HOPG in phenyl octane [29,37,38]. These authors showed that in solution at room temperature and oxygen-free environment, imidazole did not coordinate with NiOEP even when the imidazole was present in a 50:1 molar excess, Fig. 6a. However, when the same compound is supported on HOPG, significant binding to nickel occurs. Consider the reaction at the phenyloctane/HOPG interface at 25 °C, as shown in Fig. 6. STM images of a NiOEP monolayer

before (b) and after (c) the addition of 1.5 mM Im which produced a $\Theta = 0.5$ coverage. The Im–NiOEP adduct molecules appear as bright spots in Fig. 6c. Time dependent imaging showed that the binding of Im to the nickel ion is reversible and that the average coverage is constant, demonstrating dynamic equilibrium. Similar to the previous work on CoOEP + O_2 at the solution/HOPG interface, the axial coordination of Im to NiOEP was effectively described by the Langmuir adsorption model. The Langmuir isotherm fit the data well and gave an equilibrium constant, $K_c = \Theta/(1-\Theta)(c/c^0)$, where c^0 is 1 M. Nandi et al. defined the standard Gibbs free energy to be $\Delta G_c^0 = -RT \ln(K_c)$ and found $\Delta G_c^0 = -15.8$ kJ/mol. They estimated the standard reaction entropy, ΔS_c^0, to be −216 J/mol·K, which resulted in $\Delta H_c^0 = -80$ kJ/mol. These values are comparable to the thermodynamic parameters obtained for Im binding to metalloporphyrins in solution environments [52,53].

Using DFT simulations Nandi et al. showed that the Im ligation process is supported by charge donation from the HOPG surface to Im molecules via NiOEP monolayer [29,38]. Additionally, they showed that the nickel ion in the Im–NiOEP/HOPG complex was in a singlet ground state. This was an unexpected result since previous experimental studies found triplet ground states for the five and six coordinated Im–nickel(II) porphyrins in the gas-phase or in solution. Calculations also predicted that in the Im–NiOEP/HOPG complex, Im acts as a π-acceptor ligand instead of a σ–donor. Such a ligation of Im to NiOEP was different from literature reports regarding imidazole binding to Ni porphyrins in solution [55].

Fig. 7 shows charge redistribution at the NiOEP/HOPG and Im–NiOEP/HOPG interfaces. For the NiOEP/HOPG interface, positive charge (Fig. 7, a1 and a2) is mostly located on the NiOEP monolayer and in its vicinity, whereas negative charge (Fig.7, b1 nad b2) is located on the HOPG substrate. But in the Im−NiOEP/HOPG interface, the positive charge (Fig. 7, c1 nad c2) is reduced on the Im−NiOEP monolayer in comparison to negative charge (Fig.7, D1 and D2). In the Im−NiOEP/HOPG case, there is almost no negative charge on HOPG (Fig.7, d1 and d2) and a small positive charge. Quantitative charge redistribution calculations for HOPG at the NiOEP/HOPG interface showed a gain of ∼0.1 e for each NiOEP molecule while in Im−NiOEP/HOPG, HOPG donated ∼0.4 e to each Im−NiOEP complex. Thus, HOPG acts as an acceptor of charge from NiOEP without imidazole but as a donor when Im−NiOEP is the adsorbate. The 0.4 e charge donated by HOPG to Im−NiOEP is shared only a little with the NiOEP receptor and mostly goes to the ligand (∼0.3 e). This was an unexpected result because imidazole is usually assumed to be a two-electron donor. However when Im binds to NiOEP on HOPG, it acts as a π-electron acceptor. HOPG in turn acts as a charge donor.

Unlike nickel porphyrin, which binds two axial ligands, the zinc porphyrins can bind only a single axial ligand to form five-coordinate complexes in solution. At the solution/solid interface, however, the Zn porphyrins receptors formed well-ordered monolayers that more readily bound exogenous nitrogenous ligands than in solution.

ZnTPD, Zn 5,10,15,20-*meso*-tetradodecyl porphyrin, Zn(II), at the tetradecane/HOPG interface, was found to coordinate 3-nitropyridine more effectively than in fluid solution by Feringa and coworkers [32]. Their studies under ambient conditions revealed that the ratio of ligated ZnTDP to the uncoordinated porphyrin was higher at the tetradecane/HOPG interface than in the tetradecane solution. This enhanced binding of the axial ligand at the solution/solid interface was attributed to surface effects. Feringa also reported a qualitative observation of time

dependent binding dynamics for single nitropyridines within large domains containing 90% coordinated ZnTDP molecules [32].

Chilukuri explored the binding of 4,4'-bipyridine (bpy) to ZnOEP at the octyl benzene/HOPG interface at room temperature in argon atmosphere [54]. He determined that the porphyrin receptors exhibited affinity toward the ligand and that the bpy binding/dissociation events could be readily tracked in successive STM scans, at different ligand concentrations. Uncoordinated ZnOEP molecules were identifiable by their dim centers while the ligated bpy–ZnOEP species appeared bright (see example Fig. 8). Ligand binding/dissociation sites in figures 8b and 8c are circled; white circles indicate the unbound Zn ions in both frames; the green circles are bright molecules that were dim in the previous image; new dim molecules identified by blue rings.

To estimate the relative binding energies of ZnOEP and bpy–ZnOEP to HOPG Chilukuri performed DFT calculations of pyridine (py) and zinc porphine as models [54]. The binding energy was calculated to be ~58 kJ/mol. This value matched well with the experimental binding enthalpy (~38 kJ/mole) of ZnTPP with pyridine molecule in benzene solution [55]. On HOPG surface, Chilukuri calculated the zinc porphine–py binding energy to be ~80 kJ/mol. The significant increase in the calculated binding energy of the surface adsorbed Zn coordinated complex compared to its binding enthalpy in solution strongly supports the participation of the substrate in the py binding events.

Otsuki et al. reported the binding of 4-(phenylazo)pyridine (azo) to 5,10,15,20-tetrakis(4-octadecyloxyphenyl) porphyrin, Zn(C_{18}OPP), at the phenyloctane/HOPG interface [30]. To better identify the coordinated molecules, Otsuki added the azo ligand (*trans* isomer) to a 50:50 mixture of Zn(C_{18}OPP) and H_2(C_{18}OPP) (free–base form of the porphyrin). The ligated Zn porphyrins immediately became observable as bright features in the STM images, while the free–base receptors remained dim. Based on the observed apparent heights of the Zn(C_{18}OPP)–azo and H_2(C_{18}OPP) species it was possible to discriminate between *trans* and *cis*–azo coordinated Zn ions when a respective 2:3 ratio of the ligand isomers was added to the porphyrin receptor at the phenyloctane/HOPG interface. The authors noted that the binding/dissociation kinetics of the processes they investigated were much faster than the time scale of their STM instrument [30].

CONCLUSIONS AND OUTLOOK

Reports on probing reversible porphyrin receptor–ligand binding events at the solution/solid interface illustrate the remarkable power of single molecule microscopy in acquiring both qualitative and quantitative information about molecule binding affinity, reaction equilibrium kinetics and thermodynamics. The solution/solid interface provides a dynamic environment where reaction rates can be controlled by varying solution pH, temperature and reactant concentration. With the electrochemical STM, one can also precisely control the redox chemistry of ligand binding/dissociation to adsorbed porphyrin receptors.

Metal porphyrins do not share the same ligand binding chemistry on conducting surfaces and in solution. We have shown examples of chemically responsive systems that are not stable in solution but are stable on a conducting support. Additionally, similar ligand–receptor/substrate systems exhibited different behavior under applied potential and with no potential control.

Electronic communication between the substrate and the adsorbed porphyrin influenced the receptor's affinity toward an exogenous ligand and in some cases modified the donor/acceptor characteristics of the bound ligand. Substrate moderated receptor reactivity can also lead to cooperativity, sometimes called synergism or allostery. Cooperativity occurs when the binding of one molecule to a receptor enhances (or weakens) the binding of other ligands to adjacent receptors. This behavior has been observed experimentally at the solution/solid interface [23] and calculations have verified cooperative effects [56] in chemically relevant processes on surfaces. More studies (experimental and theoretical) are underway to better understand the role of the substrate in cooperative ligand binding to metal porphyrins at the solution/solid interface [57].

Binding and dissociation processes are characterized not only by the equilibrium constants, but also by how fast association/dissociation occurs. STM based studies of reversible chemical reactions are defined by the instrumental time resolution. Typically, an image of few tens of nanometers square takes seconds of acquisition time. This period can be considered slow when compared to some binding/dissociation reaction half-lives. Still, there are a wealth of reversible process with reaction rates that are compatible with scan time constrains of current commercial STMs. When a reaction proceeds slowly, STM sequential imaging can provide very valuable information about reaction mechanism as well kinetics and thermodynamics. Monitoring kinetics of short-lived events requires video–frequency scanning. Development of STMs that can operate at video–rate [15] is in progress but such instruments have not yet been routinely employed in reactivity studies at the solution/solid interface. For studying fast reaction kinetics, the STM measurements will need to be coupled with high-speed statistical measurements based on optical techniques or surface plasmon resonance.

Computational studies are an important adjunct to the understanding of ligand binding chemistry at the solution/solid interface. We have shown that calculations can determine the electronic and chemical properties of the porphyrin receptor/substrate interactions and estimate the charge redistribution in the ligand–porphyrin receptor/substrate system. Future theoretical investigations need to address the fundamental origins of ligand–porphyrin receptor/support adsorption energies and substrate induced receptor cooperativity. Consideration of the solvent is also important as it plays a role in both enthalpy and entropy. Solvent can also potentially bond with both the ligand and receptor and directly alter the binding kinetics.

The combination of faster STM sampling experiments with atomistic details and advanced computations will bring a more complete view of chemical and biological reversible binding processes. Deeper understanding of binding will enable more rational design of sensors, pharmaceuticals and catalysts.

ACKNOWLEDGEMENTS

This report is based on work supported by the National Science Foundation under grant CHE-1800070. We gratefully acknowledge their support.

REFERENCES

1 Lucas MF, Rousseau DL and Guallar V. *Biochim. Biophys. Acta* 2011; **1807**: 1305-1313.

2 Robertson A and Shinkai S. *Coord. Chem. Rev.* 2000 **205**: 157-199.

3 Kadish KM, Rerriera G, Smith KM and Guilard R. Handbook of Porphyrin Science: With Applications to Chemistry, Physics, Materials Science, Engineering, Biology and Medicine. HemeBiochemistry. Volume 26, World Scientific. World Scientific Publishing Company (2013) ISBN-10: 981430718.

4 Liu JY, Li XF, Guo ZX, Li YZ Huang A J and Chang WB. *J. Mol. Catal. A: Chemical* 2002 **179**: 27-33.

5 Kadish KM, Rerriera G, Smith KM and Guilard R. Handbook of Porphyrin Science: With Applications to Chemistry, Physics, Materials Science, Engineering, Biology and Medicine. Catalysis and Bio-inspired systems. Volume 10, World Scientific. World Scientific Publishing Company (2010) ISBN-10: 9814307181

6 Smith AR and Klosek JA. *Fuel Processing Technology* 2001 **70**: 115–134.

7 Zhao-Karger Z, Gao P, Ebert T, Klyatskaya S, Chen, Z, Ruben M and Fichtne M. *Adv. Mater.* 2019 **31**: 1806599/1-7.

8 Paolesse R, Nardis S, Monti D, Stefanelli M, and Di Natale C. *Chem. Rev.* 2017; **117**: 2517- 2583;

9 Batinic-Haberle I, Tovmasyan A and Spasojevic I, *Antioxidants & Redox Signaling* 2018; **29**: 1691-1724;

10 Khan R, Özkan M, Khaligh A and Tuncel D. *Photochem. Photobiol. Sci.* 2019, **18**: 1147-1155.

11 Nakagaki S, Ferreira GKB, Ucoski GA and de Freitas Castro KA. *Molecules* 2013; **18***:* 7279-7308.

12 Barona-Castano JC, Carmona-Vargas CC, Brocksom TJ and de Oliveira KT. *Molecules* 2016; **21**: 310-337.

13 Hipps KW and Scudiero L. *J. Chem. Educ.* 2005; **82**: 704-711.

14 Moore AM and Weiss PS. A*nnual Rev. Anal. Chem.* 2008; **1**: 2008 857-882.

15 Li Q and Lu Q. *Rev. Sci. Instrument* 2011; **82**: 053705/1-053705/4.

16 Gottfried JM. *Surf. Sci. Rep.* 2015; **70**: 259-379.

17 Otsuki J. *Coord. Chem. Rev.* 2010; **254**: 2311-2341.

18 Hieringer W, Flechtner K, Kretschmann A, Seufert K, Auwarter W, Barth JV, Gorling A, Steinruck HP and Gottfried JM. *J. Am. Chem. Soc.* 2011; **133**: 6206-6222.

19 Auwarter W, Ecjia D, Klappenberger F and Barth JV. *Nature Chem.* 2015; **7**:105-120.

20 Seufert K, Auwaurter W and Barth JV. *J. Am. Chem. Soc.* 2010; **132**: 18141-18146.

21 Flechtner K, Kretschmann A, Bradshaw LR, Walz MM, Steinruck HP and Gottfried JM. *J. Phys. Chem. C* 2007; **111**: 5821-5824.

22 Gottfried JM and Marbach H. *Z. Phys. Chem.* 2009; **223**: 53-74.

23 Munninghoff JAW and Elemans JAAW. *Chem. Commun.* 2017; **53**:1769-1788.

24 den Boer D, Li M, Habets T, Iavicoli P, Rowan AE, Nolte RJM, Speller S, Amabilino DB, De Feyter S and Elemans JAAW, *Nature Chem.* 2013; **5**: 621-627.

25 Gu JY, Cai ZF, Wang D and Wan LJ. *ACS Nano* 2016; **10**: 8746-8750.

26 Friesen BA, Bhattarai A, Hipps KW and Mazur U. *J. Amer. Chem. Soc.* 2012; **134**: 14897-14904.

27 Cai ZF, Wang X, Wang D and Wan LJ. *ChemElectroChem* 2016; **3**: 2048-2051.

28 Hao Y, Robert S, Weatherup RS, Baran Eren B, Gabor A, Somorjai GA and Salmeron M. *Langmuir* 2016; 32: 5526-5531.

29 Nandi G, Chilukuri B, Hipps KW and Mazur U. *PhysChemChemPhys* 2016; **18**: 20819-20829.

30 Otsuki J, Seki E, Taguchi T, Asakawa M and Miyake K. *Chem. Lett.* 2007; **36**: 740-741.

31 Ferreira Q, Alcacer L and Morgado J. *Nanotechnology* 2011; **22**: 435604-435614.

32 Visser J, Katsonis N, Vicario J and Feringa BL. *Langmuir* 2009; **25**: 5980-5985.

33 Bhattarai A, Hipps KW and Mazur U. *J. Am. Chem. Soc.* 2014; **136**: 2142-2148.

34 Bhattarai A, Mazur U and Hipps KW. *J. Phys. Chem. C* 2015; **119**: 9386-9394.

35 Jahanbekam A Mazur U Hipps KW. *Rev. Sci. Instrum.* 2014; **85**: 103701-103701.

36 Hulsken B, van Hameren R, Gerristen JW, Khoury TL, Thordarson P, Crosslet MJ, Roeland AR, Nolte JM, Elemans JAAW and Speller S. *Nature Nanotech.* 2007; **2**: 285-289.

37 Mazur U and Hipps KW. *Chem. Commun.* 2015; **51**: 4737-4749.

38 Hipps KW and Mazur U. *Langmuir* 2018; **34**: 3-17.

39 Collman JP, Brauman JI, Doxsee KM, Halbert TR, Hayes SE and Suslick KS. *J. Am. Chem. Soc.* 1978; **100**: 2761-2766.

40 Collman JP, Yan YL, Eberspacher T, Xie X and Solomon JI. *Inorg. Chem.* 2005; **44**: 9628-9630.

41 Wang YH, Schneider PE, Goldsmith ZK, Mondal B, Hammes-Schiffer S and Stahl SS. *ACS Cent. Sci.* 2019; **5**: 1024-1034.

42 Zhou Y, Xing YF, Wen J, Ma HB, Wang FB and Xia XH. *Sci. Bulletin* 2019; **64**: 1158-1166.

43 Kadish KM, Shao J, Ou Z, Fremond L, Zhan R, Burdet F, Barbe JM, Gros CP and Guilard R. *Inorg. Chem.* 2005; **44**: 6744-6754.

44 Masa J, Ozoemenab K, Schuhmanna W and Zagal JH. *J. Porph. Phthal.* 2012; **16**: 761-784.

45 De Wael K and Adriaens A. *Talanta* 2008; **74**: 1562-1567.

46 Yoshimoto S Inukai J Tada A Abe T Morimoto T Osuka A Furuta| H Itaya K. *J. Phys. Chem. B* 2004; **108**; 1948-1954.

47 Wang X, Cai ZF, Wang D and Wan LJ. *J. Amer. Chem. Soc.* 2019; **141**: 7665-7669.

48 Scudiero L, Barlow DE, Mazur U and Hipps KW. *J. Am. Chem. Soc.* 2001; **123**: 4073-4080.

49 Jia SL, Jentzen W, Shang M, Song XZ, Ma JG, Scheidt WR and Shelnutt JA. *Inorg. Chem.* 1998; **37**: 4402-4412.

50 Kaplan WK, Scott RA and Suslick KS. *J. Am. Chem. Soc.* 1990; **112**: 1283-1285.

51 Shibayama N, Inubushi T, Morimoto H and Yonetani T. *Biochemistry* 1987; **26**: 2194-2201.

52 Pasternak PF, Spiro GE and Teach M. *J. Inorg. Nucl. Chem.* 1974; **36**: 599-606.

53 Ciaccio PR, Ellis JV, Munson ME, Kedderis GL, McConville FX and Duclos JM. *J. Inorg. Nucl. Chem.* 1976; **38**: 1885-1889.

54 Chilukuri B, Hipps KW and Mazur U. Work in progress.

55 Cole SJ, Curthoys GC, Magnusson EA and Phillips JN. *Inorg. Chem*. 1972; **11**: 1024-1028.

56 Chilukuri B, Mazur U and Hipps KW. *PhysChemChemPhys* 2019; **21**: 10505-10513.

57 Korpany K, Chilukuri B, Hipps KW and Mazur U. Work in progress.

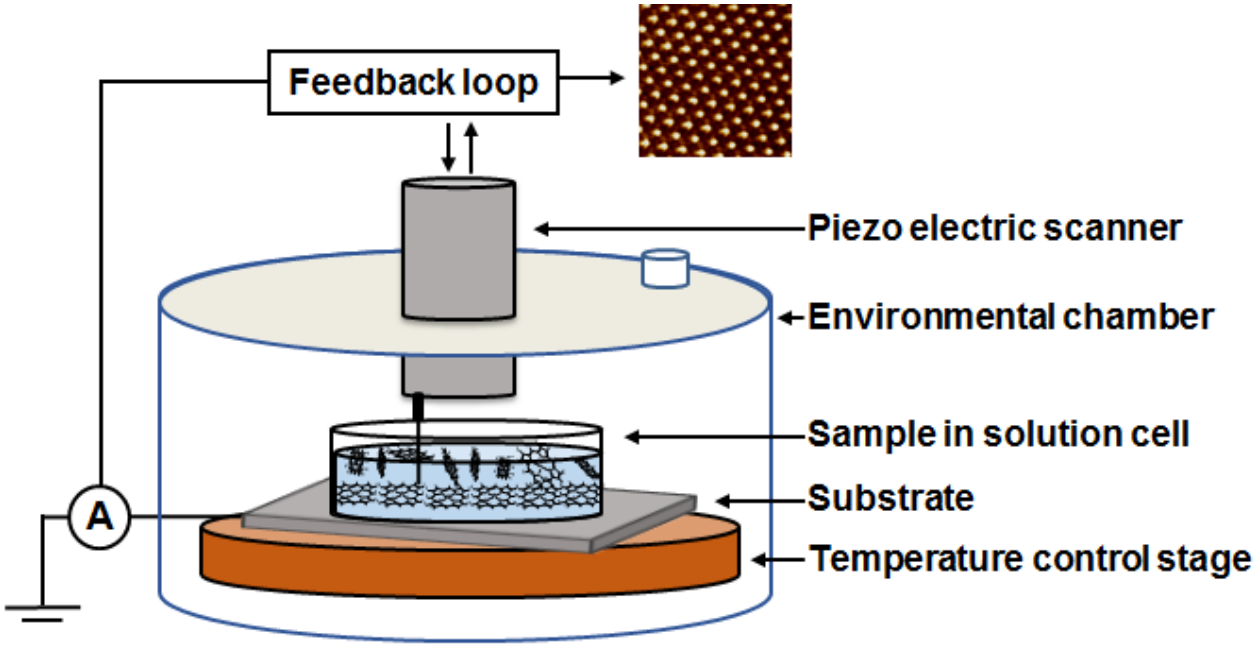
Feedback loop
Piezo electric scanner
Environmental chamber
Sample in solution cell
Substrate
Temperature control stage
A

Fig. 1.

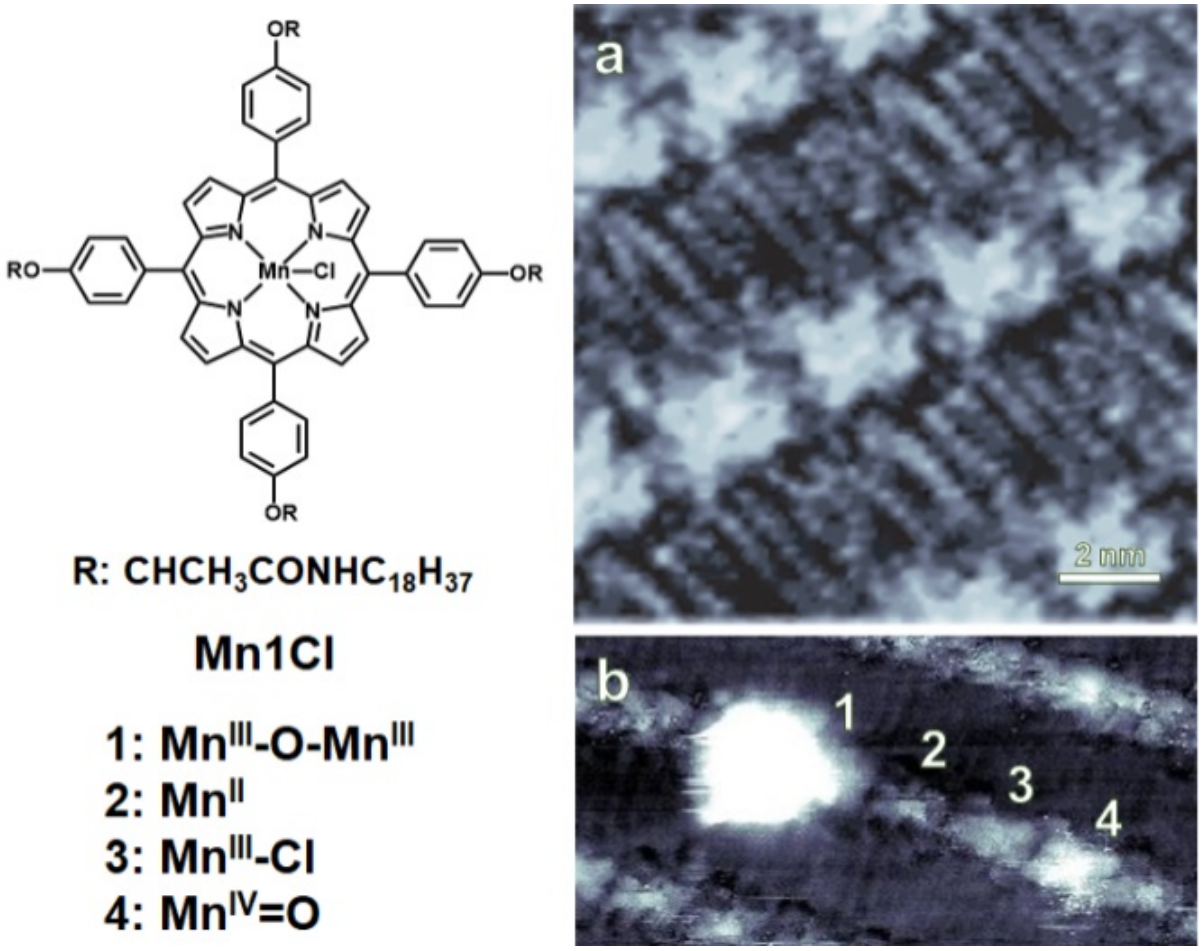
OR
RO
OR
Mn—Cl
N
OR
R: CHCH3CONHC18H37
Mn1Cl
1: MnIII-O-MnIII
2: MnII
3: MnIII-Cl
4: MnIV=O
a
2 nm
b
1
2
3
4

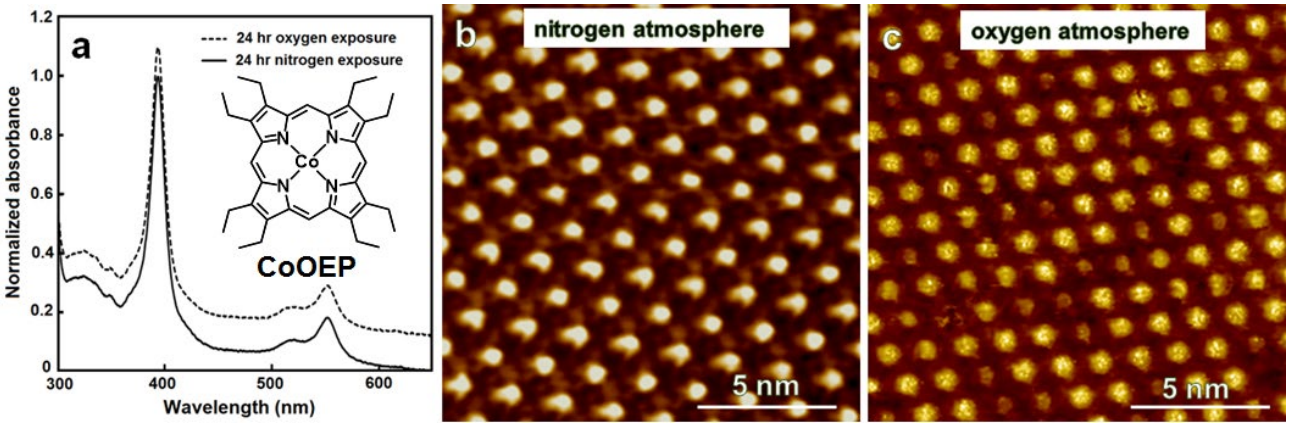
a
24 hr oxygen exposure
24 hr nitrogen exposure
Normalized absorbance
Wavelength (nm)
CoOEP
b
nitrogen atmosphere
5 nm
c
oxygen atmosphere
5 nm

Fig. 2.

Fig. 3.

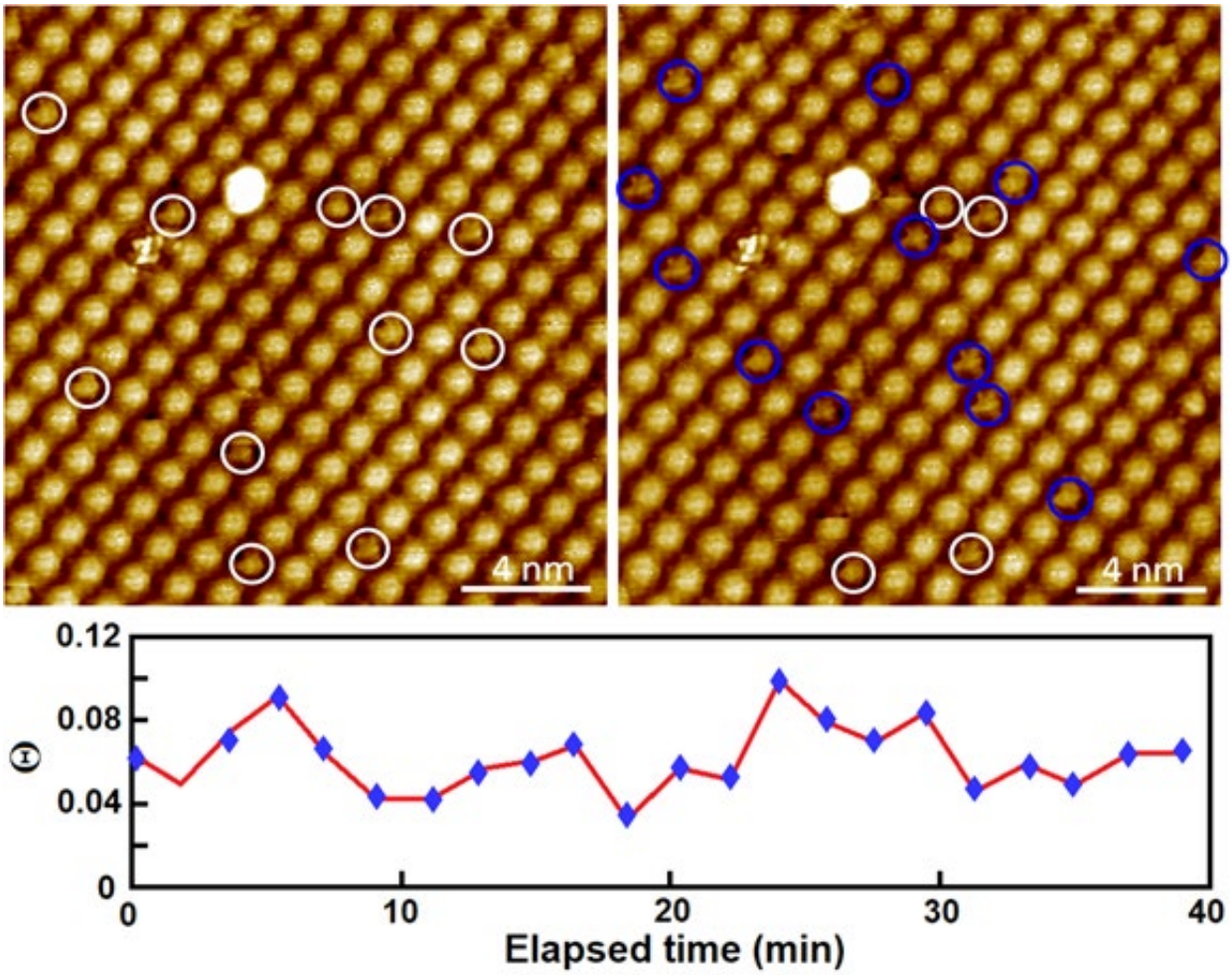
4 nm
4 nm
0.12
0.08
0.04
0
Θ
0
10
20
30
40
Elapsed time (min)

Fig. 4.

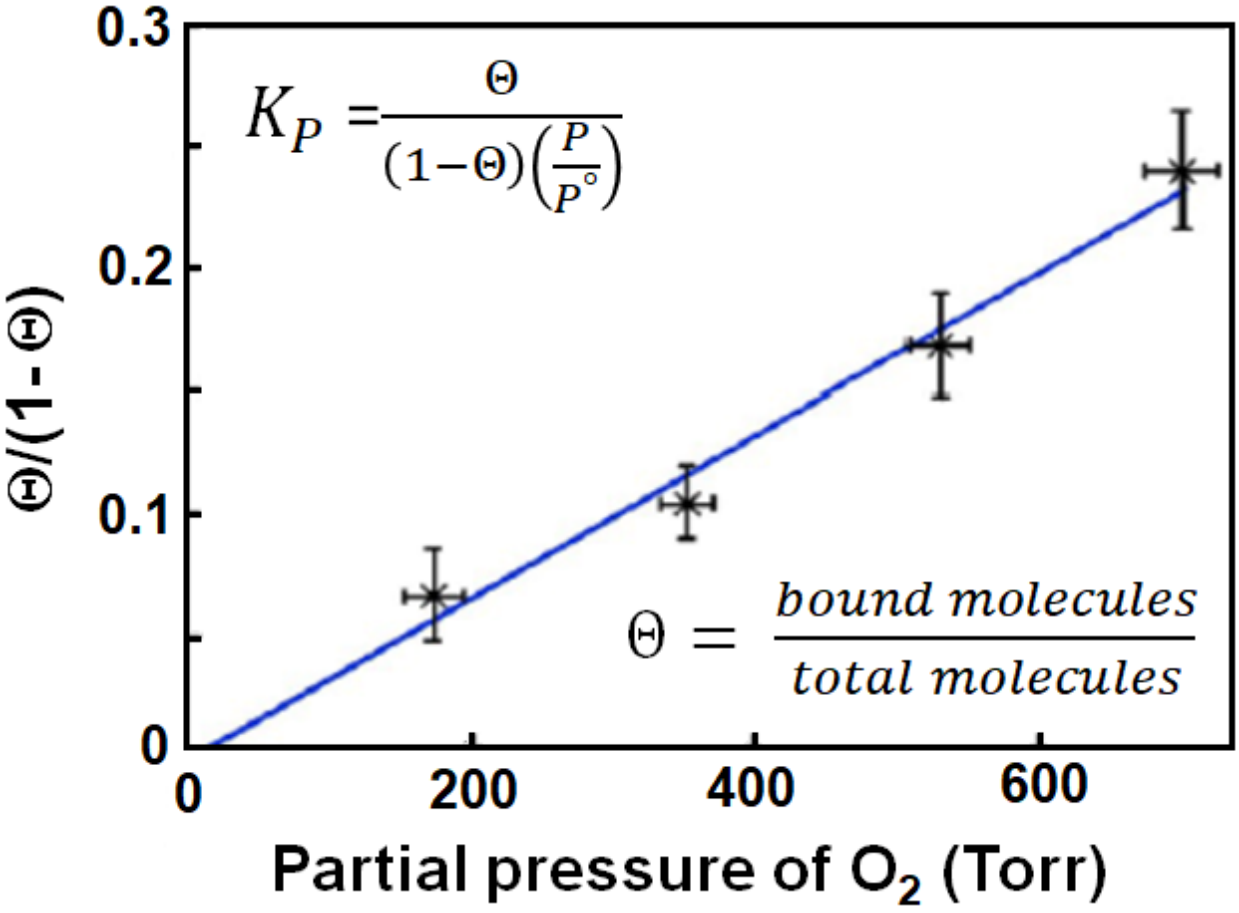
$K_P = \frac{\Theta}{(1-\Theta)\left(\frac{P}{P^\circ}\right)}$
$\Theta = \frac{bound\ molecules}{total\ molecules}$
Θ/(1 - Θ)
0.3
0.2
0.1
0
0
200
400
600
Partial pressure of O_2 (Torr)

Fig 5.

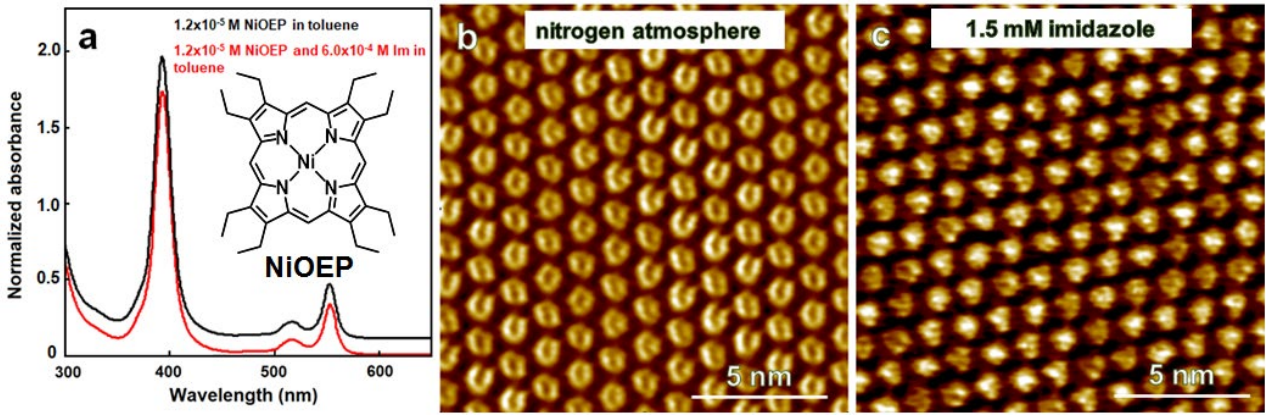
a
1.2x10-5 M NiOEP in toluene
1.2x10-5 M NiOEP and 6.0x10-4 M Im in toluene
NiOEP
Normalized absorbance
Wavelength (nm)
b
nitrogen atmosphere
5 nm
c
1.5 mM imidazole
5 nm

Fig 6.

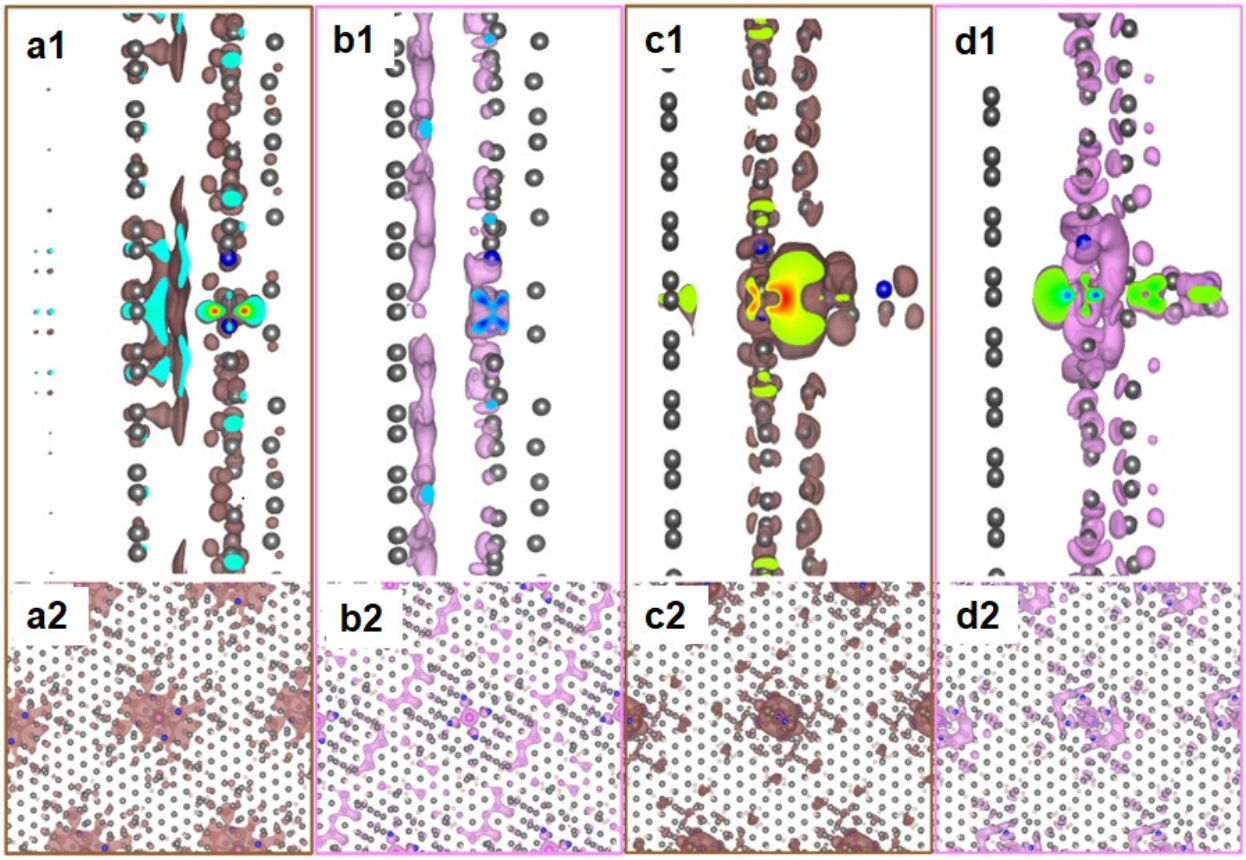

Fig. 7.

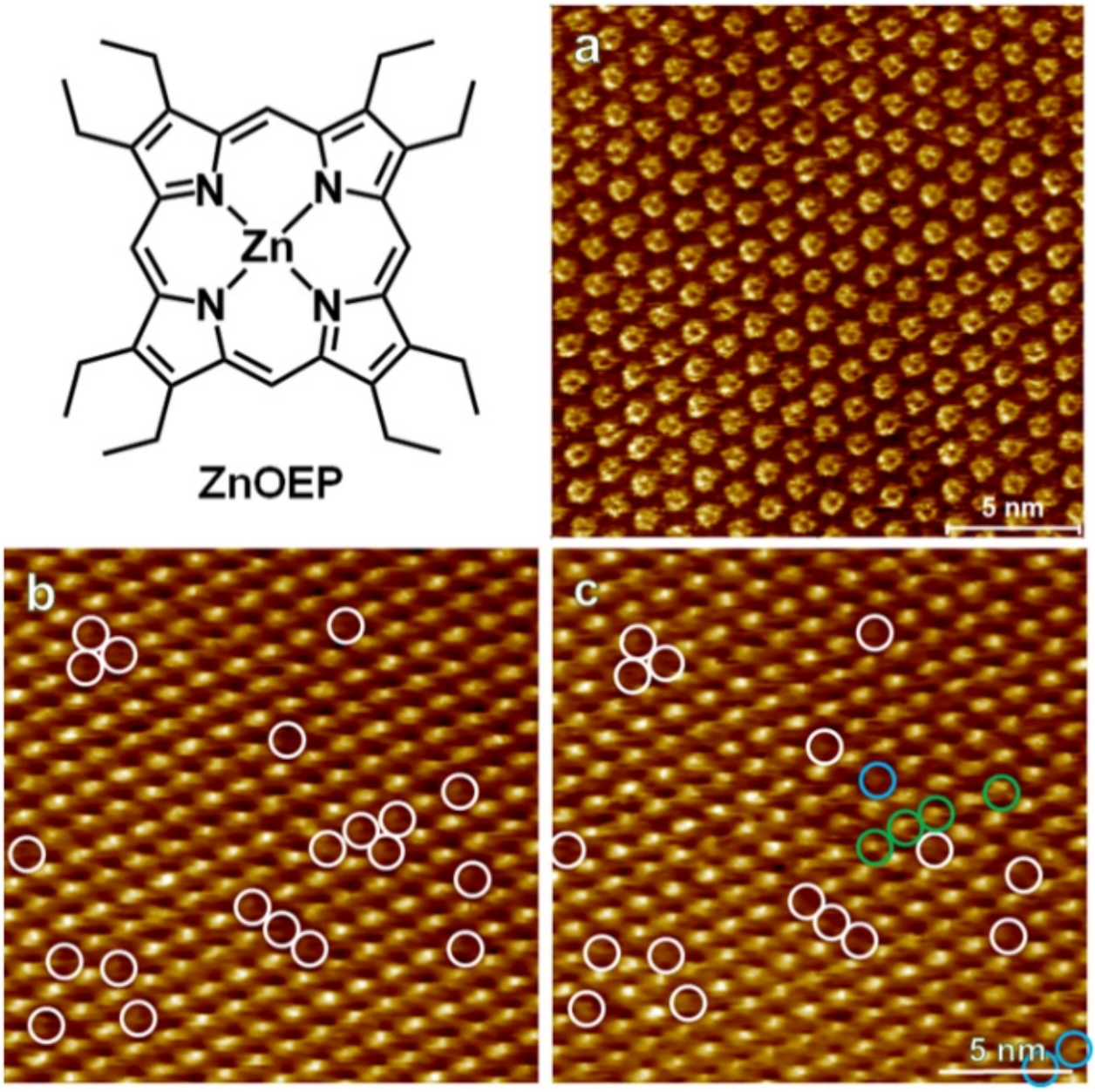

Fig. 8.

Fig. 1. A schematic of an STM experimental setup for imaging at the liquid/solid interface. The solution cell can hold up to 50 μL of fluid solution. The enclosed environmental chamber allows for varying the atmosphere and temperature is controlled with the Peltier heating/cooling stage

Fig. 2. STM images of a monolayer of Mn1Cl at the 1-octanoic acid/Au(111) interface under (a) an argon atmosphere and (b) in air at 25 °C. The image taken in air showed four different species labeled 1 through 4; their assignments are provided on the left side of the image. Tunneling parameters: V_{bias} = –0.8 V, I_{set} = 10 pA. Reproduced in part from reference 23. Copyright *Nat. Chem.* 2013

Fig. 3. UV−vis spectrum of CoOEP in toluene solution after 24 h exposure to O_2 (offset) and to N_2, respectively (a). Constant current STM images of the phenyloctane/CoOEP/HOPG interface under conditions of N_2 (b) and O_2 (c) saturation at 25 °C. STM data were acquired at −0.5 V and 20 pA set point. Some molecules in (c) are considerably dimer than others – these are oxygen ligated CoOEP species

Fig. 4. Time evolution of oxygen coverage on the CoOEP/HOPG surface in phenyl octane solvent. Θ is the fraction of CoOEP sites occupied by O_2 in a given frame. Two sequential STM images shown were used in generating the data points. Circled molecules indicate oxygen binding sites. Reproduced in part from reference 25. Copyright American Chemical Society

Fig. 5. Langmuir plot of relative surface coverage of dark molecules as a function of O_2 partial pressure at 25 °C

Fig. 6. UV−vis spectrum of NiOEP in toluene solution N_2, (a). Constant current STM images of the phenyloctane/NiOEP/HOPG interface under conditions of N_2 (b) and 1.5 mM imidazole (c) at 25 °C. STM data (b) was acquired at 0.6 V and 20 pA set point and image (c) was obtained at 0.2 V and 50 pA. Note that some molecules in (c) have bright centers – these are imidazole ligated NiOEP species

Fig. 7. From left to right, charge density difference mappings for positive (colored in brown) and negative (colored in pink) charges for NiOEP/HOPG (A and B) and Im–NiOEP/HOPG (C and D) systems respectively. The images in the top row represent side-view and the bottom rows represent top-view. Element colors are carbon–gray, nitrogen–blue, nickel–yellow. The rainbow colors indicate charge with blue being highly negative and red being highly positive. Reproduced from reference 36. Copyright American Chemical Society

Fig. 8. Constant current STM image of the ZnOEP monolayer at the phenyloctane/HOPG interface, (a). Two sequential STM images after excess of 4,4'-bipyridine added to the ZnOEP/HOPG in octyl benzene, (b) and (c). Circled molecules indicate bpy deficient sites. Data was acquired under argon at 25 °C